J A

# Vertical Muon Intensity Measured with MACRO at Gran Sasso Laboratory

*The MACRO Collaboration*

**INFN - Laboratori Nazionali del Gran Sasso**

# Vertical Muon Intensity Measured with MACRO at the Gran Sasso Laboratory

## The MACRO Collaboration

M. Ambrosio[12], R. Antolini[7], G. Auriemma[14,a], R. Baker[11], A. Baldini[13], G. C. Barbarino[12], B. C. Barish[4], G. Battistoni[6,b], R. Bellotti[1], C. Bemporad[13], P. Bernardini[10], H. Bilokon[6], V. Bisi[16], C. Bloise[6], C. Bower[8], S. Bussino[14], F. Cafagna[1], M. Calicchio[1], D. Campana[12], M. Carboni[6]. M. Castellano[1], S. Cecchini[2,c], F. Cei[13,d], P. Celio[14], V. Chiarella[6], A. Corona[14], S. Coutu[11], G. De Cataldo[1], H. Dekhissi[2,e], C. De Marzo[1], I. De Mitri[9], M. De Vincenzi[14,f], A. Di Credico[7,14], O. Erriquez[1], C. Favuzzi[1], C. Forti[6], P. Fusco[1], G. Giacomelli[2], G. Giannini[13,g], N. Giglietto[1], M. Grassi[13], A. Grillo[7], F. Guarino[12], P. Guarnaccia[1], C. Gustavino[7], A. Habig[8], K. Hanson[11], A. Hawthorne[8], R. Heinz[8], J. T. Hong[3], E. Iarocci[6,h], E. Katsavounidis[4], E. Kearns[3], S. Kyriazopoulou[4], E. Lamanna[14], C. Lane[5], D. S. Levin[11], P. Lipari[14], R. Liu[4], N. Longley[4], M. J. Longo[11], Y. Lu[15], G. Ludlam[3], G. Mancarella[10], G. Mandrioli[2], A. Margiotta-Neri[2], A. Marini[6], D. Martello[10], A. Marzari-Chiesa[16], M. N. Mazziotta[1], D. G. Michael[4], S. Mikheyev[7,i], L. Miller[8], M. Mittelbrunn[5], P. Monacelli[9], T. Montaruli[1], M. Monteno[16], S. Mufson[8], J. Musser[8], D. Nicoló[13,d], R. Nolty[4], C. Okada[3], C. Orth[3], G. Osteria[12]. O. Palamara[10], S. Parlati[7], V. Patera[6,h], L. Patrizii[2], R. Pazzi[13], C. W. Peck[4], S. Petrera[10], N. D. Pignatano[4], P. Pistilli[10], V. Popa[2,l], A. Rainó[1], J. Reynoldson[7], F. Ronga[6], A. Sanzgiri[15], F. Sartogo[14], C. Satriano[14,a], L. Satta[6,h], E. Scapparone[2], K. Scholberg[4], A. Sciubba[6,h], P. Serra-Lugaresi[2], M. Severi[14], M. Sitta[16]. P. Spinelli[1], M. Spinetti[6], M. Spurio[2], R. Steinberg[5], J. L. Stone[3], L.R. Sulak[3], A. Surdo[10], G. Tarlé[11], F. Tassoni[14], V. Togo[2], V. Valente[6], C. W. Walter[4] and R. Webb[15]

1. Dipartimento di Fisica dell'Università di Bari and INFN, 70126 Bari, Italy
2. Dipartimento di Fisica dell'Università di Bologna and INFN, 40126 Bologna, Italy
3. Physics Department, Boston University, Boston, MA 02215, USA
4. California Institute of Technology, Pasadena, CA 91125, USA
5. Department of Physics, Drexel University, Philadelphia, PA 19104, USA
6. Laboratori Nazionali di Frascati dell'INFN, 00044 Frascati (Roma), Italy
7. Laboratori Nazionali del Gran Sasso dell'INFN, 67010 Assergi (L'Aquila), Italy
8. Depts. of Physics and of Astronomy, Indiana University, Bloomington, IN 47405, USA
9. Dipartimento di Fisica dell'Università dell'Aquila and INFN, 67100 L'Aquila, Italy
10. Dipartimento di Fisica dell'Università di Lecce and INFN, 73100 Lecce, Italy
11. Department of Physics, University of Michigan, Ann Arbor, MI 48109, USA
12. Dipartimento di Fisica dell'Università di Napoli and INFN, 80125 Napoli, Italy
13. Dipartimento di Fisica dell'Università di Pisa and INFN, 56010 Pisa, Italy
14. Dipartimento di Fisica dell'Università di Roma "La Sapienza" and INFN, 00185 Roma, Italy
15. Physics Department, Texas A&M University, College Station, TX 77843, USA
16. Dipartimento di Fisica Sperimentale dell'Università di Torino and INFN, 10125 Torino, Italy
   a Also Università della Basilicata, 85100 Potenza, Italy
   b Also INFN Milano, 20133 Milano, Italy
   c Also Istituto TESRE/CNR, 40129 Bologna, Italy
   d Also Scuola Normale Superiore di Pisa, 56010 Pisa, Italy
   e Also Faculty of Sciences, University Mohamed I, B.P. 424 Oujda, Morocco
   f Also Dipartimento di Fisica, Università di Roma III, Roma, Italy
   g Also Università di Trieste and INFN, 34100 Trieste, Italy

*h* Also Dipartimento di Energetica, Università di Roma, 00185 Roma, Italy

*i* Also Institute for Nuclear Research, Russian Academy of Science, 117312 Moscow, Russia

*l* Also Institute for Atomic Physics, 76900 Bucharest, Romania

## Abstract

We report new results on the vertical muon intensity, on the primary "all-nucleon" spectrum and on the surface muon flux. The data were obtained in $\sim 500$ days of data taking with the lower MACRO detector at the Gran Sasso Laboratory. A comparison with the world data is also presented.

# 1. Introduction

Measurements of the underground muon intensity still provide the main information on the energy spectrum of atmospheric muons above 1 TeV and yield information on the "all-nucleon" spectrum of the primary cosmic radiation. They also constrain models of atmospheric showers, through both the muon vertical intensity slope and the absolute normalization. Further information on atmospheric processes may be obtained from the measurement of the underground muon intensity versus the zenith angle $\theta$. As suggested by several authors, the production of prompt muons in atmospheric showers should modify the $\sec(\theta)$ angular distribution characteristic of pion and kaon decays and interactions [1, 2, 3].

In this paper we present new measurements of the underground muon intensity in the energy range $1-20$ TeV, corresponding to a primary energy $10-200$ TeV/nucleon, performed with the MACRO detector running at the Gran Sasso National Laboratory in central Italy. We use this measurement to extract the primary all nucleon spectrum. The analysis of prompt muon production will be the focus of a further paper.

The rock overburden has a minimum depth of 3150 hg cm$^{-2}$; its composition and topography are discussed in detail in the Appendix. The detector has been described in detail elsewhere [4], and when completed will have an acceptance of $\sim 10000$ m$^2$ sr for isotropic fluxes. A first measurement of single muon data was performed earlier with a limited portion of the detector [5] and a reduced statistics data sample which allowed the measurement of the vertical intensity up to 5200 hg cm$^{-2}$.

# 2. Vertical muon intensity

The present analysis refers to data collected with the lower part of MACRO with an acceptance of $S\Omega \simeq 3100$ m$^2$ sr for atmospheric muons. The lower structure consists of six nearly identical units, called supermodules, of 12m $\times$ 12m $\times$ 4.8m. Each supermodule consists of ten horizontal planes of streamer tubes, 12m $\times$ 12m. The eight innermost planes are separated by seven layers of $\simeq 60$ g cm$^{-2}$ absorbers of low activity Gran Sasso rock. The two outermost planes are separated by two 19 cm layers

of liquid scintillator. The lateral walls consist of stacked tanks of liquid scintillator, 25 cm thick, sandwiched between six vertical streamer tubes planes.

All streamer tube wires are read out, providing the X coordinate on the horizontal planes and the Z coordinate on the vertical planes. On the horizontal planes the second coordinate, D, is obtained by reading the pulses induced on horizontal aluminum strips oriented at 26.5° with respect to the streamer tubes axis, to allow stereoscopic reconstruction. Muon tracks are thus reconstructed with an angular resolution of 0.2°. This resolution is negligible when compared to the average multiple scattering angle of 0.8° for muons crossing the overburden rock. This value is consistent with the angular differences measured between parallel muons belonging to the same event detected in MACRO.

Data were collected in a 500 day period, starting in July 1991, when the apparatus was still under construction, using only the streamer tube system. The hardware trigger was defined by either six streamer tube planes fired anywhere, or five consecutive horizontal planes, excluding the first and the last ones. A muon track is reconstructed if at least four horizontal planes are recorded, both in the wire and strip views. The data runs were then selected as follows: runs were accepted if they had $\geq 4$ hr duration; had a dead time of less than 1%; and a counting rate per hour per supermodule inside a range of $\pm 3\sigma$ around the mean value. After these cuts, we have $3.91 \times 10^6$ muons surviving over a live time of 4228 hours. These statistics are thus more than one order of magnitude larger than those reported in Reference [5]. The large statistics of this sample allows us to also study the Gran Sasso rock systematics and to reject angular regions where the muon intensities are not compatible with the measured average intensities of the regions with the same nominal rock thickness.

The total data sample (single and multiple muons) is used to determine the bin-by-bin vertical muon intensity $I(h, \theta, \phi)$ as:

$$I(h, \theta, \phi) = \left(\frac{1}{\Delta T}\right) \frac{\Sigma_i N_i m_i}{\Sigma_j \Delta \Omega_j A_j \epsilon_j / \cos \theta_j} \tag{1}$$

where $\Delta T$ is the live time; $N_i$ is the number of observed events of muon multiplicity $m_i$ in the bin of slant depth h, taken from the military topographical map of the mountain described in the Appendix; $A_j$ is the geometric detector projected area for that bin; $\epsilon_j$ is the combined trigger and reconstruction efficiency and $\theta_j$ is the muon zenith angle. The data is binned with $\Delta \theta = 1°$ , $\Delta \phi = 2°$.

The projected area $A_j(\theta, \phi)$ and the detector tracking efficiency $\epsilon_j(\theta, \phi)$ were calculated from a detailed Monte Carlo based on GEANT [6] to produce simulated data which were processed through the same offline chain used for real data. For each bin the Gran Sasso rock thickness in meters was converted to standard rock slant depth (hg cm$^{-2}$) using the Gran Sasso rock parameters listed in Table 4, and a conversion formula described in Reference [7].

The solid angle bins were then divided into 54 bins of equal slant depth h and width $\Delta h = 50$ hg cm$^{-2}$ in the range $3200 < h < 4750$ hg cm$^{-2}$, $\Delta h = 100$ hg cm$^{-2}$ thereafter until $h = 6950$ hg cm$^{-2}$. The measured vertical muon intensity as a function of the slant depth h, for the zenith range 0° – 60°, is reported in Table 1 and is shown in Figure 1. Each point is the mean value of the $I(h, \theta, \phi)$ distribution at fixed slant depth h.

3

| Depth | $I(h) \pm \Delta I(h)$ | Depth | $I(h) \pm \Delta I(h)$ |
|---|---|---|---|
| 3200 | $(2.00 \pm 0.01) \times 10^{-8}$ | 4550 | $(3.29 \pm 0.07) \times 10^{-9}$ |
| 3250 | $(1.85 \pm 0.01) \times 10^{-8}$ | 4600 | $(3.05 \pm 0.07) \times 10^{-9}$ |
| 3300 | $(1.73 \pm 0.01) \times 10^{-8}$ | 4650 | $(2.92 \pm 0.04) \times 10^{-9}$ |
| 3350 | $(1.59 \pm 0.01) \times 10^{-8}$ | 4700 | $(2.72 \pm 0.06) \times 10^{-9}$ |
| 3400 | $(1.48 \pm 0.01) \times 10^{-8}$ | 4762 | $(2.61 \pm 0.04) \times 10^{-9}$ |
| 3450 | $(1.39 \pm 0.01) \times 10^{-8}$ | 4850 | $(2.32 \pm 0.06) \times 10^{-9}$ |
| 3500 | $(1.30 \pm 0.01) \times 10^{-8}$ | 4950 | $(2.02 \pm 0.06) \times 10^{-9}$ |
| 3550 | $(1.215 \pm 0.008) \times 10^{-8}$ | 5050 | $(1.86 \pm 0.03) \times 10^{-9}$ |
| 3600 | $(1.144 \pm 0.008) \times 10^{-8}$ | 5150 | $(1.60 \pm 0.04) \times 10^{-9}$ |
| 3650 | $(1.058 \pm 0.007) \times 10^{-8}$ | 5250 | $(1.40 \pm 0.02) \times 10^{-9}$ |
| 3700 | $(1.000 \pm 0.007) \times 10^{-8}$ | 5350 | $(1.28 \pm 0.04) \times 10^{-9}$ |
| 3750 | $(9.44 \pm 0.07) \times 10^{-9}$ | 5450 | $(1.05 \pm 0.03) \times 10^{-9}$ |
| 3800 | $(8.85 \pm 0.06) \times 10^{-9}$ | 5550 | $(9.6 \pm 0.2) \times 10^{-10}$ |
| 3850 | $(8.23 \pm 0.06) \times 10^{-9}$ | 5650 | $(8.7 \pm 0.2) \times 10^{-10}$ |
| 3900 | $(7.73 \pm 0.07) \times 10^{-9}$ | 5750 | $(7.5 \pm 0.1) \times 10^{-10}$ |
| 3950 | $(7.20 \pm 0.07) \times 10^{-9}$ | 5850 | $(6.8 \pm 0.2) \times 10^{-10}$ |
| 4000 | $(6.75 \pm 0.06) \times 10^{-9}$ | 5950 | $(5.8 \pm 0.5) \times 10^{-10}$ |
| 4050 | $(6.37 \pm 0.06) \times 10^{-9}$ | 6050 | $(5.2 \pm 0.3) \times 10^{-10}$ |
| 4100 | $(5.88 \pm 0.06) \times 10^{-9}$ | 6150 | $(4.6 \pm 0.2) \times 10^{-10}$ |
| 4150 | $(5.49 \pm 0.06) \times 10^{-9}$ | 6250 | $(4.3 \pm 0.1) \times 10^{-10}$ |
| 4200 | $(5.15 \pm 0.05) \times 10^{-9}$ | 6350 | $(3.6 \pm 0.7) \times 10^{-10}$ |
| 4250 | $(4.82 \pm 0.06) \times 10^{-9}$ | 6450 | $(3.2 \pm 0.4) \times 10^{-10}$ |
| 4300 | $(4.51 \pm 0.05) \times 10^{-9}$ | 6550 | $(2.7 \pm 0.3) \times 10^{-10}$ |
| 4350 | $(4.21 \pm 0.07) \times 10^{-9}$ | 6650 | $(2.7 \pm 0.5) \times 10^{-10}$ |
| 4400 | $(3.94 \pm 0.07) \times 10^{-9}$ | 6750 | $(2.2 \pm 0.3) \times 10^{-10}$ |
| 4450 | $(3.69 \pm 0.09) \times 10^{-9}$ | 6850 | $(2.2 \pm 0.3) \times 10^{-10}$ |
| 4500 | $(3.46 \pm 0.03) \times 10^{-9}$ | 6950 | $(2.0 \pm 0.3) \times 10^{-10}$ |

Table 1: Measured vertical muon underground intensity in $cm^{-2}$ $s^{-1}$ $sr^{-1}$. Slant depths are in standard rock (hg $cm^{-2}$). The quoted errors take into account the statistical uncertainties and the topographical map resolution. The additional estimated systematic scale uncertainty is $\pm 8\%$, see text.
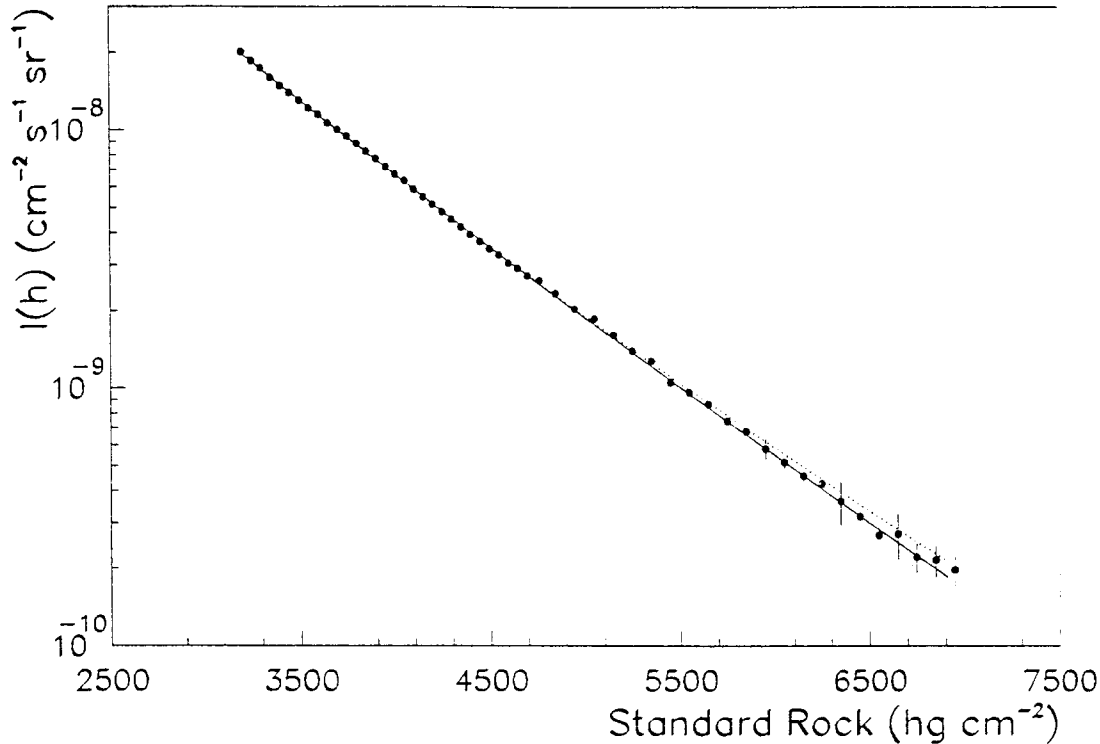
Figure 1: Measured vertical muon intensity versus standard rock (black points). The dotted and solid lines are the two and three parameter fits described in the text.

The study of the point to point uncertainties, due to the knowledge of the topographical map, produced the cut of angular regions with intensities $\pm 3\sigma$ from the average in the same slant depth as reported in the Appendix. Applications of this cut reduced our data sample by 33%, giving $2.62 \times 10^6$ muons in the final sample.

We explored the effects of the main sources of systematics. The use of an average rock density (estimated using the results of the borehole surveys of the mountain) instead of a function depending on the zenithal and azimuthal angles, contributes $\sim \pm 1.5\%$ to the rock thickness, corresponding to $\sim \pm 5\%$ on the muon intensity at 3200 hg cm$^{-2}$. A further $\sim 5\%$ contribution to the absolute scale of the muon intensity comes from the assumption of a homogeneous mountain instead of a layered structure as modelled in Reference [10] and described in [8]. The total systematic uncertainty is thus estimated at $\pm 8\%$.

In the range 3200 – 7000 hg cm$^{-2}$ the data are well fitted by the three parameter empirical formula

$$I(h) = A \left(\frac{h_0}{h}\right)^\alpha e^{-\frac{h}{h_0}} \tag{2}$$

where A = $(1.96 \pm 0.03) \times 10^{-6}$ cm$^{-2}$s$^{-1}$sr$^{-1}$, $\alpha = 1.10 \pm 0.01$ and $h_0 = (972 \pm 3)$ hg cm$^{-2}$ with a $\chi^2/\text{DoF} = 65/51$. Using the Frejus [9] function

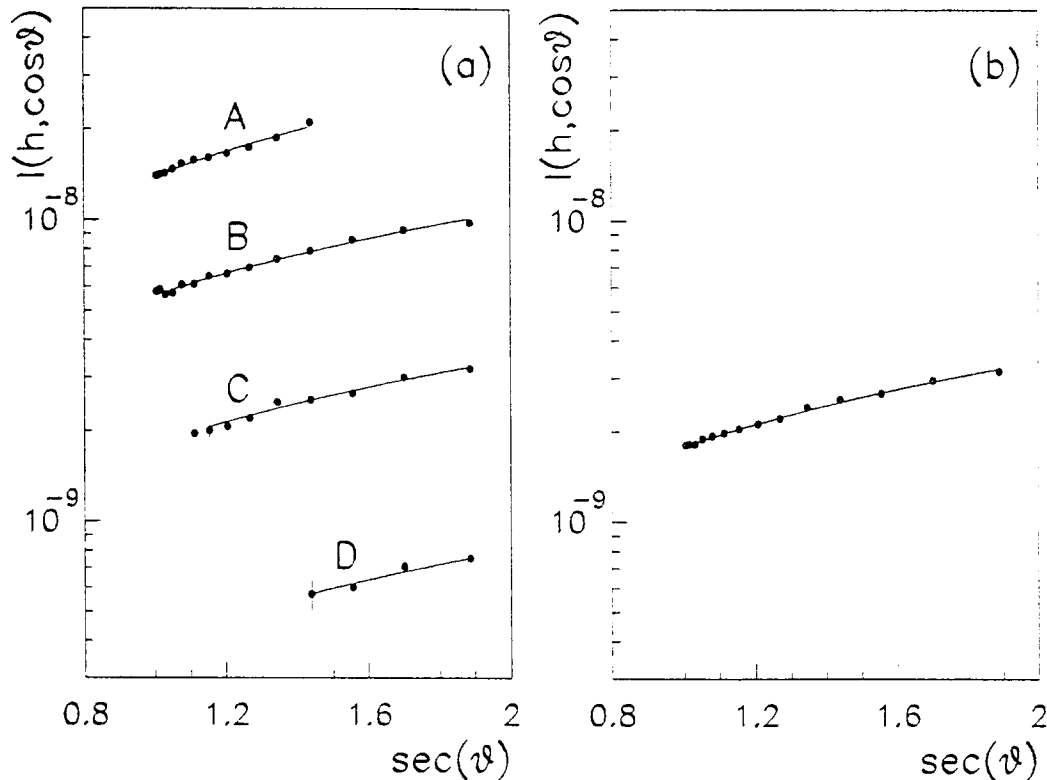$$I(h) = B \left(\frac{h_1}{h}\right)^2 e^{-\frac{h}{h_1}} \tag{3}$$

5

Figure 2: (a) The vertical muon intensity versus $1/\cos(\theta)$ is presented for 4 ranges of rock depth: A) 3150 – 3750; B) 3850 – 4550; C) 4650 – 5550; D) 5650 – 6950 hg cm$^{-2}$. (b) The data shown in part (a) are scaled to h = 5400 hg cm$^{-2}$. Data are plotted in logarithmic scale.

in the same range, we obtain B = $(1.81 \pm 0.06) \times 10^{-6}$ cm$^{-2}$s$^{-1}$sr$^{-1}$ and $h_1 = (1231 \pm 1)$ hg cm$^{-2}$ with a $\chi^2/DoF = 76/52$, and a correlation coefficient between $h_1$ and B of -0.909. The errors quoted for the fitted parameters account for the statistical uncertainties and the Gran Sasso map resolution of $\sim 10$ m. Figure 2 shows the behaviour of the intensity as a function of sec($\theta$) at fixed depth. In Figure 2a the data were binned in four depth regions of rock and in Figure 2b the experimental points are scaled to the central slant depth value h = 5400 hg cm$^{-2}$ from the empirical relation (2). The errors are due to statistics and to the resolution of the topographical map; the systematic contributions related to the mountain knowledge are not included. The linear behaviour of the data is an *a posteriori* confirmation of the angular dependence of the underground muon intensity assumed in (1).

In Figure 3a our data are compared to a summary of world data in the range 1000 – 17000 hg cm$^{-2}$; Figure 3b is a blow up of the slant depth region relevant to our present results. Our data agree within the combined statistical and systematic uncertainties with the data of other experiments. In Figure 3b our fit is compared to data fits of other experiments and to the Crouch compilation presented at the Moscow 87 ICRC [11]. A difference of about 40% is found between MACRO and NUSEX fits where our data overlap [16]. The Frejus fit [9] differs from ours by $\sim 10 - 15\%$; which is within one standard deviation of their fitted parameters. The comparison of our data with the

Crouch compilation shows differences of less than 6% over this range. The observed discrepancies with NUSEX might be connected to unknown systematic uncertainties in their rock overburden.

# 3. Primary Spectrum

In the context of the superposition model, the muon flux at the surface contains information on the "all-nucleon" primary spectrum $N(E_p)$, and this information is mediated through the details of the hadronic interactions and meson lifetimes. In the energy range relevant for the present measurement (10 – 200 TeV/nucleon), the relation between the uncorrelated muon flux and the "all-nucleon" spectrum is approximated as reported in Reference [1] by the following:

$$\frac{dN_\mu}{dE\, d\Omega} \simeq N(E) \frac{Z_{N\pi}}{1 - Z_{NN}} \frac{\left[1 - (r_\pi)^{\gamma+1}\right](1 - r_\pi)^{-1}(\gamma+1)^{-1}}{1 + \frac{B_\pi \cos\theta E}{\epsilon_\pi}} \tag{4}$$

where:

$$B_\pi = \frac{(\gamma+2)}{(\gamma+1)} \frac{1 - (r_\pi)^{\gamma+1}}{1 - (r_\pi)^{\gamma+2}} \frac{\Lambda_\pi - \Lambda_N}{\Lambda_\pi ln (\Lambda_\pi/\Lambda_N)}$$

$$r_\pi = \left(\frac{m_\mu}{m_\pi}\right)^2 .$$

Equation (4) is summed over kaon decay channels as well, where we define $B_K$ and $r_K$ in a similar fashion. The constant $\epsilon_{\pi,K}$ contains the meson lifetimes and depends on the structure of the atmosphere; $Z_{ij}$ are the spectrum averaged moments , which in principle may depend on the energy; they contain information on the inclusive distribution as well as the primary spectrum; $\Lambda_i$ are the atmospheric attenuation lengths.

Assuming for the "all-nucleon" spectrum a simple power dependence

$$N(E) = N_0 E^{-\gamma_p}$$

(which is well established in the energy range pertaining to this measurement) both the spectral index, $\gamma_p$, and normalization, $N_0$, can be derived from the vertical intensity, after the spectrum averaged moments and interaction lengths (as well as details of the atmosphere) are deduced from a Monte Carlo code. In the approximation of exact Feynman scaling and a single power spectrum, the spectrum averaged moments and interaction lengths are constant.

We estimated the "all-nucleon" spectrum by the least square method to unfold $N(E)$ from the measured underground intensity defined by:

$$I(h) = \int d\Omega \int_0^\infty \frac{dN_\mu}{dE\, d\Omega} P(E, h) dE \tag{5}$$

with h the rock depth, $\frac{dN_\mu}{dE\, d\Omega}$ the muon intensity at the surface, $P(E, h)$ the survival probability, and the angular integration is performed at constant slant depth. The survival probabilities were calculated for surface muons with energies in the 1 – 100 TeV energy range, using a GEANT code especially tuned for the Gran Sasso rock. The

7
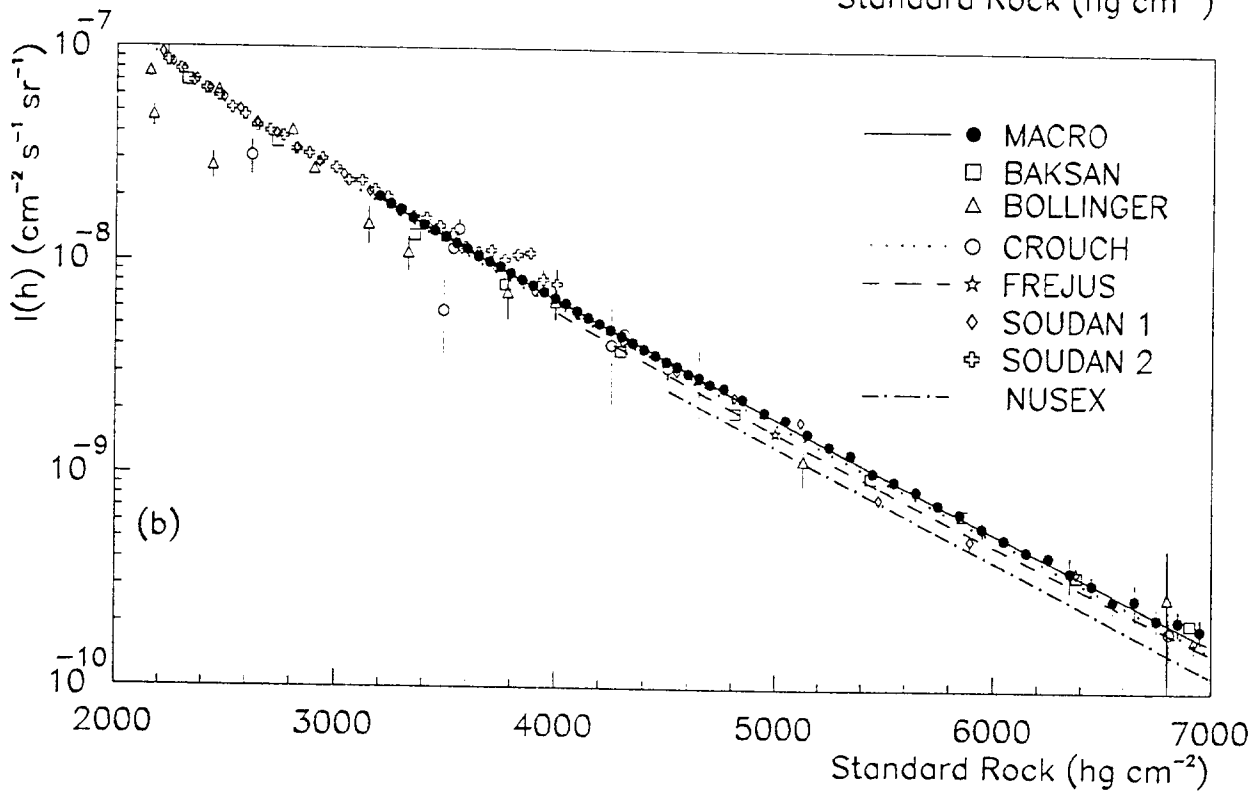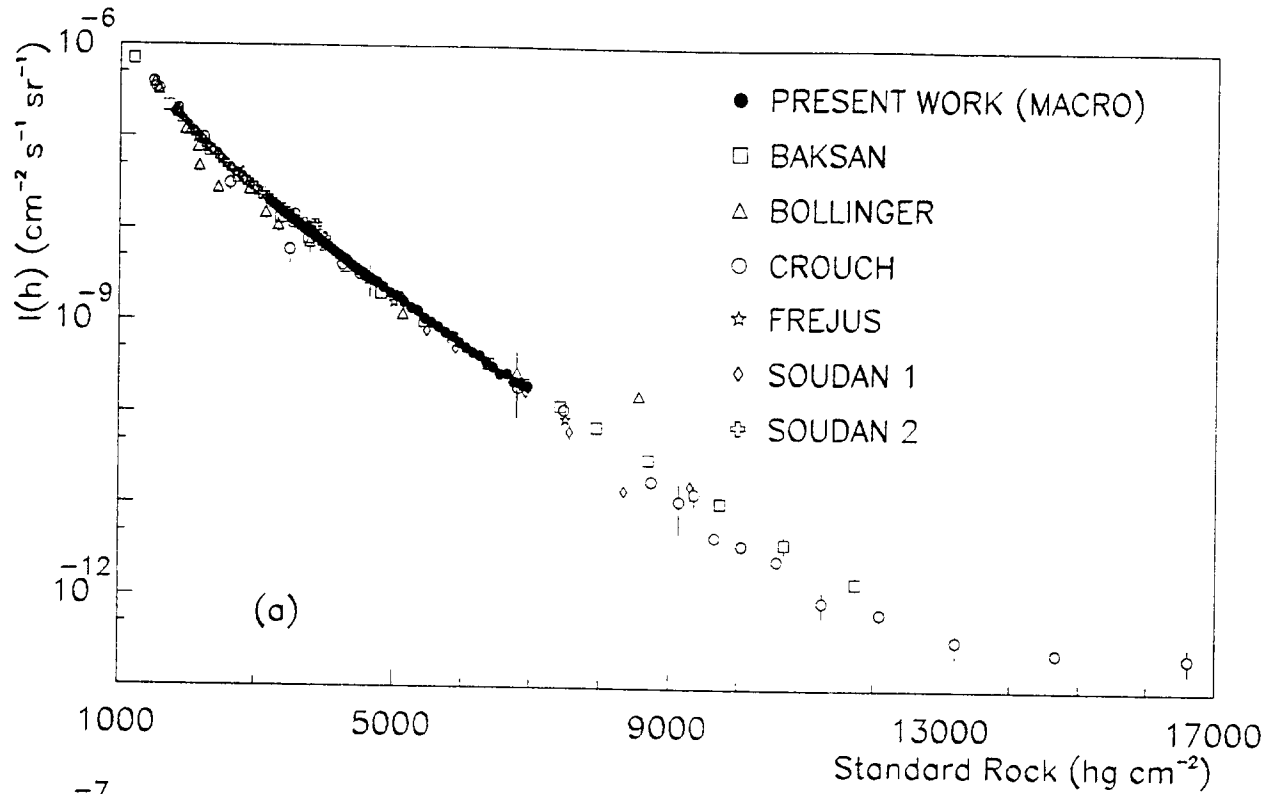
Figure 3: Vertical muon intensity versus standard rock. (a) The present MACRO results are super-imposed on the data compiled by Crouch [11] and those collected by other experiments : Baksan [12], Bollinger [13], Frejus [9], Soudan 1 [14], Soudan 2 [15]. (b) The region covered by our data is shown in more detail. The solid line is the fit of our data according to Equation (2); the dotted line is the Crouch fit [11]; the dashed line is the Frejus fit and the dash-dotted line the NUSEX fit.

8

| Model | INPUT | | | OUTPUT | |
|---|---|---|---|---|---|
| | $Z_{NN}$ | $Z_{N\pi}$ | $Z_{NK}$ | $N_0$ $(cm^{-2}s^{-1}sr^{-1}GeV^{\gamma_p-1}A)$ | $\gamma_p$ |
| Gaisser | 0.298 | 0.079 | 0.0118 | $3.4 \pm 0.1$ | $2.78 \pm 0.04$ |
| Hemas | 0.26 | 0.057 | 0.0113 | $5.0 \pm 0.1$ | $2.79 \pm 0.04$ |
| Sibyll | 0.28 | 0.068 | 0.0071 | $4.1 \pm 0.1$ | $2.77 \pm 0.05$ |
| | $\Lambda_N$ | $\Lambda_\pi$ | $\Lambda_K$ | | |
| All models | 120 | 160 | 180 | | |

Table 2: Spectrum weighted moments ($Z_{ij}$) and atmospheric attenuation lengths ($\Lambda_i$ in g cm$^{-2}$) for hadrons, and all nucleon spectrum results fitted for the three adopted models.

code includes a detailed description of muon propagation underground, and accounts for fluctuations in muon energy losses [8].

We used different sets of $Z_{ij}$ functions derived from three interaction models: a) one from Reference [1], which are constant as a function of energy since Feynman scaling is assumed to be exact, b) the HEMAS interaction model [26] and c) the SIBYLL interaction model [27]. In the latter two cases the $Z$ functions exhibit a smooth dependence on primary energy, since scaling violations are included in the quoted models. We have chosen the values at 10 TeV/nucleon, since this is roughly the most probable energy of primaries that produce the inclusive muon flux at MACRO depth. The numerical values of these parameters are listed in Table 2.

The fit of our data using the three models gives the spectral index $\gamma_p$ and the primary normalization factor for the values listed in Table 2. The correlation coefficient between $\gamma_p$ and $N_0$ is 0.975. The errors include both the statistical and the map resolution uncertainties. Further uncertainties of the order 5% in $N_0$ and 3% in $\gamma_p$ must be considered as discussed in the next section. The spread of the three values gives an estimate of the uncertainties of the magnitude of the primary flux due to the interaction model. Our evaluations are in good agreement with the estimation reported in [28]. The results in Table 2 should be considered in light of the following comments. We notice that the Z functions from HEMAS and SIBYLL, used to reproduce the observed underground muon intensity, produce a reconstructed all-nucleon spectrum higher than what can be obtained from the average of the existing direct measurements in the range $1 - 100$ TeV[29]. This is consistent with the analysis of the muon multiplicity distributions by MACRO[30], where a full simulation using the HEMAS code gave an absolute rate of events which is lower by a factor of 25% with respect to the experimental data.

## 4. Muon flux at the surface

In order to evaluate the surface muon flux, we have chosen the parameters of the model described in Reference [1], which yields the following formula:

$$\frac{dN_\mu}{dE\,d\Omega} = A \times E^{-\gamma} \times \left( \frac{1}{1 + \frac{1.1E\ cos\theta}{115\ GeV}} + \frac{0.054}{1 + \frac{1.1E\ cos\theta}{850\ GeV}} \cdot \right) \tag{6}$$

9

We have used the same method described in Section 3 to solve for A and $\gamma$. The result of this procedure gives the following values: $A = (0.26 \pm 0.01)$ cm$^{-2}$ s$^{-1}$sr$^{-1}$ GeV$^{\gamma-1}$; $\gamma = 2.78 \pm 0.01$ with a $\chi^2/\text{DoF} = 41/52$ ($\Phi$ is in cm$^{-2}$ s$^{-1}$ sr$^{-1}$ GeV$^{-1}$, and $E$ is in GeV). The errors are due to statistics and the map resolution. The fitted parameters are also affected by uncertainties of the rock density and the hard energy loss cross sections used to estimate the survival probabilities. The effect of the uncertainty in the rock density produces a variation of 3.5% in A and less than 1% in $\gamma$. Because there are uncertainties in the bremsstrahlung and photonuclear cross sections, as pointed out in [17], the results obtained here also depend upon the cross sections of the stochastic radiative processes used in GEANT. We used different sets of survival probabilities to test the sensitivity of the fitted parameters to these uncertainties. Using the energy losses described in [18], where a different photoproduction cross section is employed [19] we obtain a variation of $\simeq 2\%$ in both A and $\gamma$ but with a $\chi^2/\text{DoF} = 2.9$. We estimate the overall systematic errors resulting from rock density and hard energy loss cross sections to be $\sim 5\%$ in A and $\sim 3\%$ in $\gamma$.

As pointed out in Reference [20], the vertical sea level muon spectrum is not well known at energies greater than a few hundred GeV and even for energies below this range, the statistical and systematic errors of existing experiments are quite large ($\pm 10$ – 15 % range). Hence our high statistics measurements of the surface muon flux in the energy range from 1 – 20 TeV provide much needed new information on the high energy dependence of the sea level muon spectrum. In Figure 4a we present a collection of world data on the surface muon differential flux versus energy. The fit through our data points is represented by the continuous line. In Figure 4b the same data are presented multiplied by $E_\mu^3$ in order to eliminate the energy dependence on the flux behaviour. Our fit agrees well with the high energy measurements at sea level. The same figure also shows the differential flux calculation of Reference [1]. A maximum difference of 10 % from our result is observed at 1 TeV. Our data provide new information on the flux of muons above 1 TeV and agree well with the predictions of Reference [1].

# 5. Conclusions

We measured the underground muon intensity as a function of the slant depth, in the range 3000 – 7000 hg cm$^{-2}$, with the MACRO detector. The average parameters of the rock were estimated using the material extracted during the tunnel excavation and the mountain surveys as described in the Appendix. The high statistics of this data sample allowed identification of regions where the mountain map is not well known. Our vertical muon intensities agree well with the SOUDAN and BAKSAN data and the world compilation of Reference [11], while the Frejus [9] and the NUSEX [16] data are lower. The differences here are likely due to different methods of measurements in each of the experiments and uncertainties in the knowledge of overburden composition in the three experiments.

Using three different nuclear interaction models the primary "all-nucleon" spectrum has been evaluated in the energy range 10 – 200 TeV/nucleon. The spectral index is almost model independent while the spread in the absolute normalization is of the order of 25%, larger than the statistical uncertainty. Also, from our data we determined the
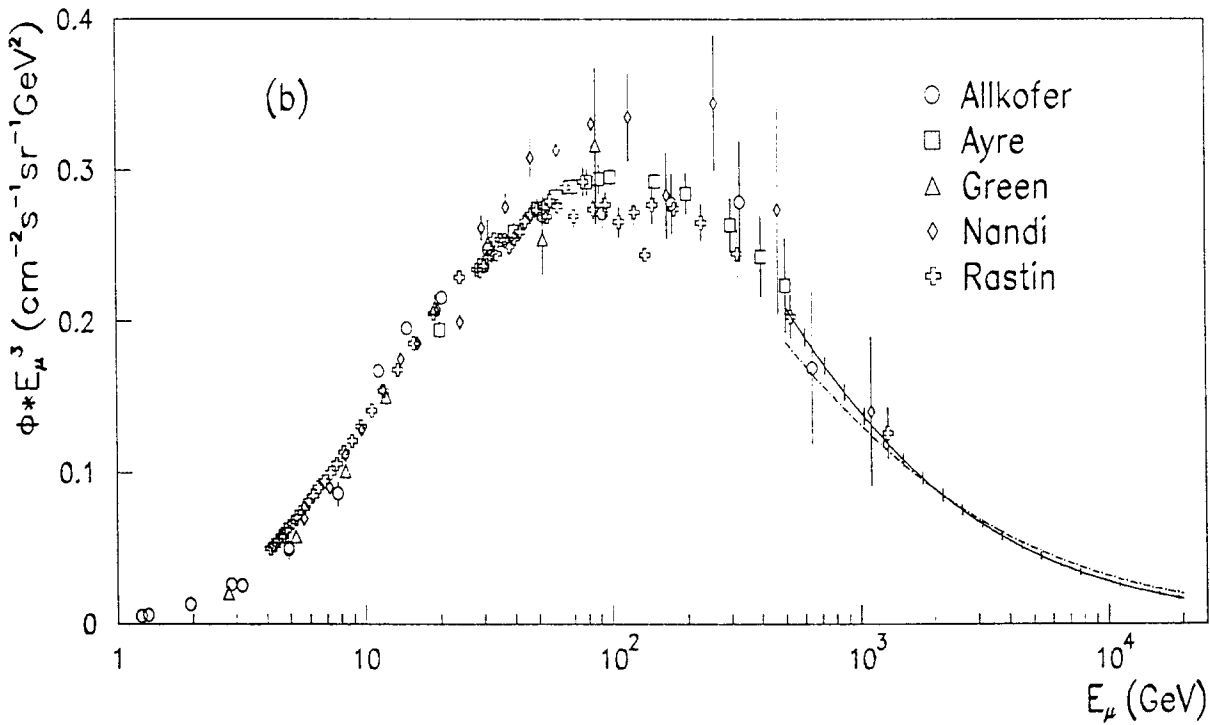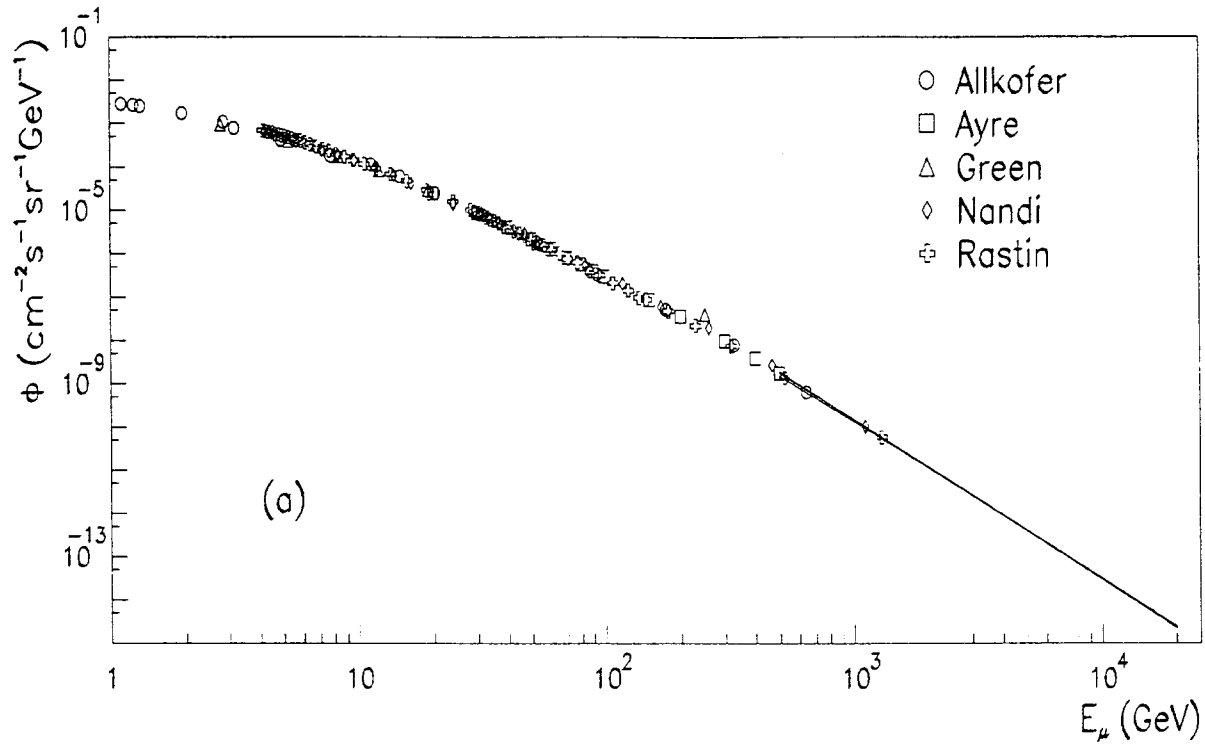
Figure 4: (a) Differential muon energy flux at the surface. The MACRO fit reported in the text (solid line) is superimposed to the available experimental measurements : Allkofer [21], Ayre [22], Green [23], Nandi [24], Rastin [25]. (b) $E_\mu^3 \Phi(E_\mu)$ is shown as a function of $E_\mu$. The solid line shows the fit of formula 6; the dash-dotted line the calculated formula pg. 71 of [1]. The vertical bars represent one standard deviation on the parameters of the fitted intensity.

surface muon flux. For muon energies larger than $\sim$ 1 TeV, our data agree well with the analytical estimate reported in [1].

The use of the MACRO detector with full acceptance will allow a considerable statistical improvement for angular regions larger than 60°, extending the statistics for depths greater than 7000 hg cm$^{-2}$, then to primary cosmic ray energies up to the knee region.

# 6. Acknowledgements

# Appendix: Characteristics of the Gran Sasso rock

The rock surrounding the Gran Sasso underground laboratory has a quite irregular structure; its composition is essentially calcareous, mixed with other materials, such as aluminum, silicon, magnesium compounds and organic remains. We made detailed analyses of the material found during the tunnel excavation to study the rock structure, and to make a composition and density model of the Gran Sasso rock [10]. The chemical composition results are shown in Table 3.

The average values of the elemental composition parameters were calculated in the angular range 0° – 60°; they are very close to the standard rock values (see Table 4). The Gran Sasso rock thicknesses as obtained from the digitization of the mountain topographic map supplied by the Italian Military Geographical Institute (IGM), as a function of the zenith and the azimuth angles, are given in Tables 5 and 6. The azimuth is measured relative to geographic North. The topographic map is not completely reliable everywhere and the empty bins represent regions where the rock is poorly known. In order to identify those regions, we employed both underground muon intensity measured with the MACRO detector using (1) and the topographic survey.

| rock type | chemical composition | % Weight |
|---|---|---|
| dolomite | $CaCO_3(90\%), MgCO_3(10\%)$ | 50 |
| dolomite limestone | $CaCO_3(50\%), MgCO_3(50\%)$ | 29 |
| flint limestone | $CaCO_3(72\%), SiO_2(8\%),$ | |
| | $Si, Al, K$ compounds (20 %) | 8 |
| karst formation | $CaCO_3$ | 9 |
| detritus | $CaCO_3(49\%), MgCO_3(1\%),$ | |
| | $Si, Al, K$ compounds (50 %) | 3 |

Table 3: Gran Sasso rock chemical composition (Reference [10]).

| A = 22.87 | Z = 11.41 | density $= (2.71 \pm 0.05)$ g cm$^{-3}$ | |
|---|---|---|---|
| Chemical element | Atomic Number | Atomic Weight | Relative Weight |
| Hydrogen | 1 | 1.008 | 0.03 |
| Carbon | 6 | 12.011 | 12.17 |
| Oxygen | 8 | 15.99 | 50.77 |
| Magnesium | 12 | 24.305 | 8.32 |
| Aluminium | 13 | 26.981 | 0.63 |
| Silicon | 14 | 28.085 | 1.05 |
| Potassium | 19 | 39.098 | 0.10 |
| Calcium | 20 | 40.078 | 26.89 |

Table 4: Gran Sasso rock average parameters. They are very similar to the so called Standard Rock for which A = 22; Z = 11 and $\rho = 2.65$ g cm$^{-3}$ .

| Azimuth | Zenith angle (degrees) | | | | | | | | | | | |
|---|---|---|---|---|---|---|---|---|---|---|---|---|
| (deg.) | 5 | 10 | 15 | 20 | 25 | 30 | 35 | 40 | 45 | 50 | 55 | 60 |
| 0 | 1338 | 1302 | 1326 | 1292 | 1268 | 1292 | 1316 | 1324 | | | | |
| 5 | 1339 | 1303 | 1302 | 1272 | 1244 | 1267 | 1303 | 1304 | | | | |
| 10 | 1341 | 1305 | 1287 | 1254 | 1224 | 1246 | 1276 | 1295 | | | | |
| 15 | 1343 | 1305 | 1278 | 1239 | 1216 | 1221 | 1238 | 1267 | | | | |
| 20 | 1346 | 1307 | 1279 | 1237 | 1222 | 1240 | 1239 | 1234 | | | | |
| 25 | 1349 | 1310 | 1280 | 1247 | 1248 | 1272 | 1263 | 1246 | | | | |
| 30 | 1349 | 1313 | 1285 | 1271 | 1279 | 1309 | 1270 | 1277 | | | | |
| 35 | 1350 | 1317 | 1291 | 1296 | 1301 | 1298 | 1303 | 1310 | | | | |
| 40 | 1354 | 1323 | 1312 | 1320 | 1311 | 1311 | 1335 | 1343 | | | | |
| 45 | 1361 | 1336 | 1335 | 1341 | 1326 | 1344 | 1352 | 1377 | | | | |
| 50 | 1370 | 1350 | 1362 | 1374 | 1350 | 1372 | 1371 | 1378 | | | | |
| 55 | 1376 | 1359 | 1386 | 1406 | 1375 | 1364 | 1380 | 1378 | | | | |
| 60 | | | | 1414 | 1380 | 1352 | 1366 | 1370 | | | | |
| 65 | | | | 1401 | 1374 | 1337 | 1350 | 1377 | | | | |
| 70 | | | | 1390 | 1365 | 1347 | 1366 | 1383 | 1438 | 1487 | 1539 | 1597 |
| 75 | | | | 1388 | 1371 | 1371 | 1384 | 1419 | 1471 | 1516 | 1562 | 1659 |
| 80 | | | | 1398 | 1387 | 1388 | 1406 | 1465 | 1496 | 1533 | 1639 | 1774 |
| 85 | | | | 1411 | 1405 | 1414 | 1448 | 1480 | 1501 | 1592 | 1726 | 1869 |
| 90 | | | | 1420 | 1426 | 1446 | 1481 | 1495 | 1547 | 1674 | 1804 | 1908 |
| 95 | | | | 1401 | 1400 | 1430 | 1472 | 1513 | 1585 | 1649 | 1754 | 1904 |
| 100 | 1381 | 1367 | 1353 | 1380 | 1372 | 1395 | 1435 | 1482 | 1545 | 1598 | 1668 | 1805 |
| 105 | 1377 | 1358 | 1328 | 1352 | 1361 | 1353 | 1401 | 1427 | 1486 | 1557 | 1615 | 1760 |
| 110 | 1371 | 1350 | 1311 | 1330 | 1335 | 1345 | 1355 | 1398 | 1440 | 1495 | | |
| 115 | 1367 | 1341 | 1302 | 1308 | 1310 | 1317 | 1320 | 1351 | 1392 | 1455 | | |
| 120 | 1362 | 1330 | 1291 | 1280 | 1283 | 1286 | 1299 | 1317 | 1362 | 1431 | | |
| 125 | 1356 | 1314 | 1284 | 1244 | 1255 | 1255 | 1269 | 1291 | 1338 | 1410 | | |
| 130 | 1354 | 1304 | 1277 | 1232 | 1233 | 1234 | 1251 | 1268 | 1318 | 1397 | | |
| 135 | 1350 | 1287 | 1268 | 1229 | 1211 | 1214 | 1225 | 1255 | 1306 | 1380 | | |
| 140 | 1348 | 1287 | 1260 | 1223 | 1204 | 1199 | 1216 | 1246 | 1302 | 1375 | | |
| 145 | 1346 | 1284 | 1250 | 1220 | 1193 | 1190 | 1207 | 1244 | 1296 | 1370 | | |
| 150 | 1348 | 1283 | 1238 | 1215 | 1186 | 1182 | 1200 | 1241 | 1295 | 1371 | | |
| 155 | 1347 | 1280 | 1235 | 1205 | 1179 | 1173 | 1200 | 1237 | 1297 | 1371 | | |
| 160 | 1345 | 1277 | 1230 | 1203 | 1176 | 1168 | 1197 | 1236 | 1299 | 1378 | 1536 | 1764 |
| 165 | 1346 | 1271 | 1229 | 1193 | 1172 | 1164 | 1196 | 1242 | 1297 | 1385 | 1562 | 1885 |
| 170 | 1348 | 1269 | 1228 | 1185 | 1167 | 1166 | 1196 | 1250 | 1306 | 1401 | 1577 | 1974 |
| 175 | 1349 | 1268 | 1227 | 1188 | 1166 | 1165 | 1196 | 1256 | 1320 | 1414 | 1599 | 2146 |
| 180 | 1350 | 1268 | 1224 | 1192 | 1169 | 1166 | 1203 | 1260 | 1333 | 1429 | 1634 | 2142 |
| 185 | 1348 | 1268 | 1222 | 1185 | 1173 | 1171 | 1208 | 1265 | 1347 | 1451 | 1670 | 2168 |
| 190 | 1347 | 1266 | 1220 | 1183 | 1170 | 1178 | 1216 | 1271 | 1347 | 1470 | 1704 | 2085 |
| 195 | 1342 | 1260 | 1220 | 1187 | 1172 | 1186 | 1222 | 1288 | 1363 | 1486 | 1716 | 2096 |
| 200 | 1339 | 1264 | 1218 | 1186 | 1180 | 1193 | 1232 | 1298 | 1376 | 1504 | 1727 | 2023 |

Table 5: Rock thickness (m) as a function of zenith and azimuth. The table indicates the regions in the mountain where the slant depth of the overburden is known with confidence.

| Azimuth (deg.) | Zenith angle (degrees) | | | | | | | | | | | |

| Azimuth (deg.) | 5 | 10 | 15 | 20 | 25 | 30 | 35 | 40 | 45 | 50 | 55 | 60 |
|---|---|---|---|---|---|---|---|---|---|---|---|---|
| 205 | 1345 | 1266 | 1216 | 1191 | 1188 | 1203 | 1241 | 1299 | 1384 | 1521 | 1738 | 2016 |
| 210 | 1349 | 1272 | 1227 | 1198 | 1194 | 1218 | 1254 | 1307 | 1398 | 1559 | 1781 | 2243 |
| 215 | 1352 | 1277 | 1239 | 1204 | 1207 | 1228 | 1262 | 1322 | 1406 | 1575 | 1866 | 2239 |
| 220 | 1354 | 1282 | 1246 | 1210 | 1218 | 1240 | 1274 | 1334 | 1422 | 1597 | 1951 | 2227 |
| 225 | 1356 | 1292 | 1254 | 1223 | 1230 | 1260 | 1301 | 1356 | 1456 | 1637 | 1989 | 2220 |
| 230 | 1359 | 1308 | 1264 | 1251 | 1244 | 1280 | 1331 | 1397 | 1484 | 1665 | 2008 | 2225 |
| 235 | 1363 | 1322 | 1278 | 1269 | 1263 | 1285 | 1340 | 1415 | 1497 | 1679 | 2051 | 2209 |
| 240 | 1371 | 1337 | 1296 | 1292 | 1283 | 1300 | 1348 | 1424 | 1537 | 1741 | 2105 | 2286 |
| 245 | 1379 | 1337 | 1317 | 1313 | 1300 | 1317 | 1360 | 1440 | 1583 | 1784 | 2195 | 2520 |
| 250 | 1385 | 1341 | 1346 | 1332 | 1318 | 1343 | 1382 | 1462 | 1638 | 1843 | 2353 | 2630 |
| 255 | 1392 | 1348 | 1366 | 1349 | 1342 | 1369 | 1422 | 1523 | 1766 | 2042 | 2454 | 2714 |
| 260 | 1396 | 1364 | 1388 | 1368 | 1368 | 1396 | 1454 | 1567 | 1921 | 2178 | 2324 | 2520 |
| 265 | | | | 1388 | 1396 | 1426 | 1476 | 1581 | 1968 | 2056 | 2195 | 2369 |
| 270 | | | | 1409 | 1433 | 1457 | 1505 | 1587 | 1889 | 2021 | 2120 | 2303 |
| 275 | | | | 1439 | 1470 | 1499 | 1538 | 1616 | 1890 | 2012 | 2133 | 2346 |
| 280 | | | | 1465 | 1499 | 1526 | 1560 | 1639 | 1897 | 1998 | 2177 | 2394 |
| 285 | | | | 1499 | 1523 | 1560 | 1579 | 1656 | 1888 | 1996 | 2199 | 2426 |
| 290 | | | | 1532 | 1560 | 1585 | 1611 | 1713 | 1895 | 2016 | 2195 | 2462 |
| 295 | 1360 | | | 1569 | 1591 | 1622 | 1656 | 1773 | 1916 | 2035 | 2218 | 2481 |
| 300 | 1354 | | | 1597 | 1636 | 1661 | 1711 | 1849 | 1957 | 2065 | 2254 | 2609 |
| 305 | 1348 | | | 1580 | 1661 | 1699 | 1767 | 1857 | 1958 | 2094 | 2282 | 2784 |
| 310 | 1345 | | | 1543 | 1642 | 1742 | 1797 | 1866 | 2002 | 2147 | 2293 | 2835 |
| 315 | 1341 | | | 1511 | 1599 | 1742 | 1808 | 1900 | 2046 | 2206 | 2452 | 2937 |
| 320 | 1337 | | | 1477 | 1549 | 1696 | 1773 | 1887 | 2115 | 2302 | 2773 | 2960 |
| 325 | 1334 | | | | | 1651 | 1700 | 1815 | 2213 | 2571 | 2833 | 2902 |
| 330 | 1333 | | | | | 1598 | 1643 | 1738 | 2217 | 2758 | 2840 | 2922 |
| 335 | 1334 | | | | | 1537 | 1587 | 1712 | 2386 | 2723 | 2892 | 3022 |
| 340 | 1334 | | | | | 1451 | 1519 | | 2253 | 2692 | 2894 | 3038 |
| 345 | 1334 | | | | | 1385 | 1460 | | 1970 | 2494 | 2823 | 2967 |
| 350 | 1335 | | | 1326 | 1322 | 1346 | 1408 | | 1890 | 2486 | 2585 | 2881 |
| 355 | 1335 | | | 1313 | 1295 | 1320 | 1350 | | 1685 | 2180 | 2417 | 2632 |

Table 6: Rock thickness (m) as a function of zenith and azimuth. The table indicates the regions in the mountain where the slant depth of the overburden is known with confidence.

# References

[1] T. Gaisser, *Cosmic Rays and Particle Physics*, Cambridge University Press (1990).

[2] C Castagnoli *et al.*, Nuovo Cimento A, **82**, 78(1984); A. Castellina *et al.*, Nuovo Cimento C, **8**, 93(1985).

[3] L. Bergamasco *et al.*, Nuovo Cimento C, **6**, 596(1983).

[4] S.P. Ahlen *et al.*, Nucl. Instrum. Methods A, **234**, 337(1993).

[5] S.P. Ahlen *et al.*, Phys. Lett. B, **249**, 149(1990).

[6] R. Brun *et al.*, CERN GEANT 3 USER'S GUIDE DD/EE/84-1 (1987,1992).

[7] Yu. D. Kotov and V. M. Logunov, 11th ICRC, Budapest, MU-50 (1969).

[8] H. Bilokon *et al.*, *Muons survival probabilities in the Gran Sasso Rock*, LNGS - 94/92, (1994).

[9] Ch. Berger *et al.*, Phys. Rev. D, **40**, 2163(1989).

[10] P.G. Catalano, *Caratteristiche geolitologiche e strutturali dell'ammasso roccioso sovrastante il laboratorio I.N.F.N.*, ANAS report (1986); P.G. Catalano et al., Mem. Soc. Geol. It., **35**, 647(1986).

[11] M. Crouch, 20th ICRC, Moscow, HE **4.1-2** (1987).

[12] Y.M. Andreyev, V.I. Gurentsov and I.M. Kogai, 20th ICRC, Moscow, HE **4.1-19**, (1987).

[13] P.H. Barrett *et al.*, Rev. Mod. Phys., **24**, 133(1952). L. M.Bollinger, Phys. Rev. A, **79**, 207(1950).

[14] K. Ruddick, private communication and Soudan collaboration Int. Report PDK-435, (1990), (unpublished).

[15] Susan M. Kasahara Ph. D. Thesis, University of Minnesota (unpublished).

[16] M. Aglietta *et al.*, Nucl. Phys. B (Proc. Suppl.), **14**, 193(1990).

[17] R.P. Kokoulin and A.A. Petrukin, 22nd ICRC, Dublin, HE **4.1.3** (1991).

[18] P. Lipari and T. Stanev, Phys. Rev. D, **44**, 3543(1991).

[19] W. Lohmann, R. Kopp and R. Voss, *Energy loss of muons in the energy range 1–10000 GeV*, CERN 85-03 (1985).

[20] D.H. Perkins, Nucl. Phys. B, **399**, 3(1993).

[21] O.C. Allkofer, K. Carstensen and W.D. Dau, Phys. Lett. B, **36**, 425(1971).

[22] C.A. Ayre *et al.*, J. Phys. G, **1**, 584(1975).

[23] P.J. Green *et al.*, Phys. Rev. D, **20**, 1598(1979).

[24] B.C. Nandi and M.S. Sinha, J. Phys. A, **5**, 1384(1972).

[25] B.C. Rastin, J. Phys. G, **10**, 1609(1984).

[26] C. Forti *et al.*, Phys. Rev. D, **25**, 3668(1990).

[27] R.S. Fletcher, T.K. Gaisser, P. Lipari, T. Stanev, Bartol Research Institute BA-94-01, Jan 1994. Submitted to Phys. Rev. D.

[28] L. Bergamasco *et al.*, Nuovo Cimento C. **6**, 569(1983).

[29] S. Swordy, 23rd ICRC, Calgary, Invited, Rapporteur & Highlight papers, 243 (1993).

[30] M. Ambrosio *et al.*, (MACRO Collaboration), 23rd ICRC, Calgary, 2, 97 (1993).